Elementary Processes of Free-decaying Two-dimensional Turbulence in Magnetized Pure Electron Plasmas

Yosuke KAWAI and Yasuhito KIWAMOTO

Graduate School of Human and Environmental Studies, Kyoto University, Yoshidanihonmatsu-cho, Sakyo-ku, Kyoto 606-8501, Japan

(Received: 31 August 2008 / Accepted: 11 October 2008)

Elementary processes of two-dimensional (2D) turbulence have been examined by extensive analyses of fine-scale structures in the density distribution of a magnetized pure electron plasma that evolves from an unstable initial state to a single-peaked stable distribution through successive mergers of vortex patches. Fourier-based analyses have revealed that the spectral dynamics in the wave-number k space is qualitatively consistent with the theoretical picture of 2D turbulence, i.e., while the energy is transferred downward, the enstrophy cascades upward in the wave-number region larger than k_{inj} corresponding to the size of vortex patches, and the energy spectrum $E(k)$ shows a power-law scaling $k^{-\alpha}$ with $\alpha > 3$. By applying wavelet analyses to the observed density distributions, this spectral dynamics is connected directly to the vortex dynamics in the physical space. With the simultaneous resolution in the physical coordinates and wave numbers, we have observed that the enstrophy cascade is associated with the filamentation process of vortex structures. Moreover, controlled discrimination of the coherent component in terms of the wavelet coefficients indicates significant contribution of coherent vortices in steepening the energy spectrum far above the theoretical prediction of k^{-3}.

Keywords: non-neutral plasma, two-dimensional turbulence, spectral analysis, wavelet analysis

1. Introduction

In the guiding center approximation, the macroscopic dynamics of pure electron plasmas transverse to a strong magnetic field B_0 is equivalent to the two-dimensional (2D) vortex dynamics in inviscid and incompressible fluids, through the relation $\zeta = en/\varepsilon_0 B_0$ between the electron density $n(x, y)$ and the vorticity $\zeta(x, y)$ [1]. Here, $-e$ and ε_0 are the electron charge and the dielectric constant in vacuum, respectively. Taking advantage of this equivalence, many aspects of vortex dynamics constituting fundamental processes of 2D turbulence, such as the advection, merger, filamentation of vortices, has been studied extensively by employing magnetized pure electron plasmas [1, 2].

Free relaxation of 2D turbulence starting from an unstable initial distribution has also been studied, focusing on the formation of quasi-stationary states with ordered structures [1, 3, 4]. In the previous study, we have investigated the relaxation process via stochastic mergers of coherent vortices by applying time-resolved spectral analyses in terms of the density transport [5]. In this paper, we extend these examinations further to explore fundamental properties of 2D turbulence in terms of the transport of the energy and enstrophy in the wave-number k space [6].

Theoretical picture of 2D turbulence has been proposed by Kraichnan and Batchelor [7]. In these studies, they proposed that in an isotropic and homogeneous 2D turbulence, the enstrophy (vorticity) injected at the length scale of l_{inj} ($\propto 1/k_{inj}$) cascades at a constant transfer rate of η down to a scale of dissipation l_d ($\propto 1/k_d$) and dissipates at smaller scales by viscosity. This cascade picture of 2D turbulence leads to an energy spectrum characterized by the power-law scaling $E(k) \propto k^{-3}$ in the inertial range $k_{inj} \leq k \leq k_d$ of the wave-number space. In the present work, we observe the vorticity distribution $\zeta(x, y)$ in terms of the electron density distribution $n(x, y)$, and analyze the spectral dynamics over a wide range of wave numbers extending to the dissipative scale.

In addition to the Fourier-based analysis, in this paper, we also apply the wavelet analysis to the observed density distributions [8]. In contrast to the Fourier expantion, spatially localized wave packet, called "wavelet", allows us to analyze the turbulent structures in terms of both coordinate (physical space) and scale (wave-number space) simultaneously within the limits of the uncertainty principle [9]. With this advantage, we examine the spectral dynamics in the wave-number space in relation to the vortex dynamics in the physical space, and clarify characteristic features of 2D turbulence from a physical point of view.

2. Experimental Method

The experiment was carried out by using a pure electron plasma confined in a Penning-Malmberg trap with a uniform magnetic field ($B_0 = 0.048$ T) and a square-well potential. The relaxation process starts with a spontaneous formation of vortices via a nonlinear stage of the diocotron instability of a ring-shaped initial distribution [5, 10]. After the production of an initial profile, the stochastic vortex dynamics proceeds spontaneously while the electrons are held in the trap. The time evolution of the 2D density distribution was observed destructively by damping the electrons onto the conducting phosphor screen and digitizing the resultant luminosity distribution with a charge-coupled-device camera (CCD), which provides the spatial

author's e-mail: kwaiyosuke@h01a0395.mbox.media.kyoto-u.ac.jp

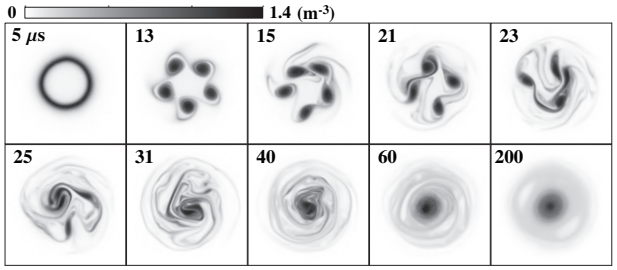

Fig. 1 Images of the time evolution of the density distribution. The darkness is proportional to the density. The time of observation (in μs) is indicated at the upper left corner.

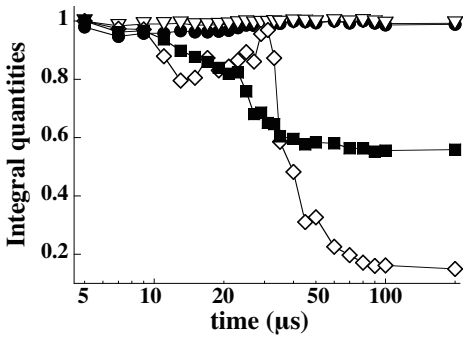

Fig. 2 Time evolution of energy E (•), total electron number N (▽), enstrophy Z_2 (■) and palinstrophy P (◊). Each integral is normalized to unity.

resolution of 0.1 mm/pix, at each time step of the relaxation. This destructive diagnostic requires a high reproducibility of the initial profiles, because of the stochastic nature of the turbulent relaxation process triggered by the instability. Therefore in this experiment, in addition to technically minimizing shot-by-shot variations in the initial profiles, an ensemble-average is applied over typically 5 shots of data for each time step in evaluating physical quantities. The details of the experimental configuration and diagnostic are reported in Refs. [2, 4–6, 11].

3. Vortex Dynamics in 2D Turbulence

The time evolution of the observed density distribution is shown in Fig. 1. Each image is denoised from instrumental noise, which is an accumulated charge on CCD pixels due to a dark current, by using the wavelet-based noise extraction method [8, 12]. The ring-shaped profile produced at 5 μs is distorted by the diocotron instability [10] within a few μs, and eventually 5 high density vortex patches are generated at 13 μs. After the formation of the first vortex patches, the successive mergers among the patches proceed spontaneously up to the formation of a single vortex, accompanied by a generation of filamentary structures that evolve toward smaller length scales. The concentrated patches rotate expelling filamentary structures from the central region, and finally form a stable distribution of a bell-shaped core profile surrounded by a low density halo at 200 μs.

This relaxation process is characterized by the integral quantities of the vorticity ($\propto n(x, y)$). Figure 2 shows the time evolution of some integrals calculated from the measured density distribution n. Each integral is normalized to unity. The calculated integrals are the electrostatic energy $E = 1/2 \int d^2\mathbf{r} n(-e\phi)$, the total electron number $N = \int d^2\mathbf{r} n$, the enstrophy $Z_2 = 1/2 \int d^2\mathbf{r} n^2$ and the palinstrophy $P = 1/2 \int d^2\mathbf{r} |\nabla n|^2$. Here, ϕ is the self electrostatic field calculated from $n(x, y)$ [11]. The palinstrophy is a measure of the fine-scale structures in the turbulence [7, 13].

Throughout the whole process, E and N do not show any systematic change except 5% variations probably attributed to shot-by-shot fluctuations in the production of the initial distributions. Therefore these integrals may be considered to be invariant. In contrast, Z_2 and P show unambiguous systematic changes. The enstrophy Z_2 undergoes a substantial decaying through the merging process, and finally goes down to 60% of the initial value. The palinstrophy P shows a rapid increase while vortex mergers are active, and is maximized at 31 μs when the filamentary structures are the most conspicuous outside the high density central region as shown in Fig. 1. After the maximization, P drops steeply, which indicates the decay of the fine-scale structures.

In order to estimate the degree of enstrophy dissipation, we evaluate an effective viscosity coefficient ν using the relation $DZ_2/Dt = -2\nu P$ derived from the Navier-Stokes equation [7, 13]. By introducing the experimental values into this equation, the effective viscosity ν is evaluated as 0.01 ± 0.003 m^{2}s^{-1}. This experimental evaluation agrees with the theoretically predicted coefficient within a factor of 3, which is estimated by introducing the parameters of the present experiment into the proposed formula [14].

4. Spectral Dynamics in 2D Turbulence

The observed vortex dynamics in the physical space corresponds to the time evolution of the energy spectrum $E(k)$ in the wave-number space shown in Fig. 3 (a). $E(k)$ is determined from the Fourier transformed density distribution $n(\mathbf{k}) = \int d^2\mathbf{r} e^{-i\mathbf{k}\cdot\mathbf{r}} n(\mathbf{r})$ as

$$E(k) = \frac{1}{2}\left(\frac{e}{\varepsilon_0 B_0}\right)^2 \int_0^{2\pi} k d\varphi \frac{|n(\mathbf{k})|^2}{k^2}, \quad (1)$$

where φ is the azimuthal angle of $\mathbf{k}$ (recall the relation $\zeta = en/\varepsilon_0 B_0$).

When the first vortex patches are generated from the ring distribution at 13 μs, the spectrum has a local maximum around the injection scale $k = k_{inj} \approx 500$ consistent with the size of the patches. Along with the subsequent mergers between patches ($t = 13 \sim 31$ μs), the energy spectrum broadens upward and shows a power-law scaling of

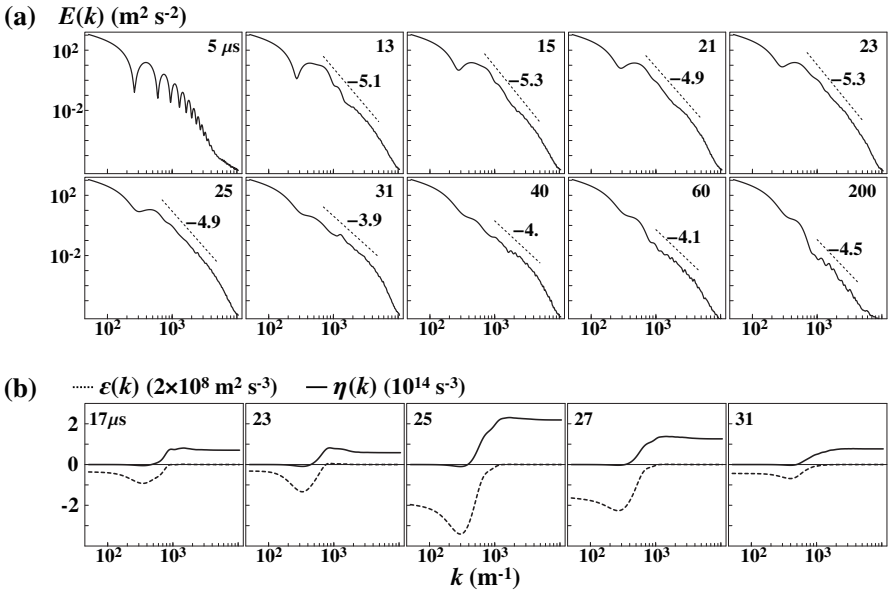

Fig. 3 (a) Time evolution of the energy spectrum calculated from the measured density distributions. Numbers at the upper left corner stand for the time of the observation. (b) Time evolution of the upward transfer rates of the energy $\varepsilon(k)$ (dashed line) and enstrophy $\eta(k)$ (solid line) through k.

$k^{-\alpha}$ in the wave-number region larger than k_{inj}. The slope of the spectrum in the interval $700 \leq k \leq 5000$ is drawn in Fig. 3 (a). Throughout the merging process, the power index α remains around 5, apparently larger than the theoretically predicted value of 3 [7]. In the decaying phase associated with the reduction in the palinstrophy ($t > 31$ μs), the energy decreases steeply in the large wave-number region of $k > 1000$, and concentrates at $k = k_{core} \approx 300$ which corresponds to the size of the core in the final state ($t = 200$ μs).

The upward transfer rate of the energy $\varepsilon(k)$ through k is evaluated from the time-resolved energy spectra in Fig. 3 (a) as

$$\varepsilon(k) = -\int_{k_{min}}^{k} dk \, \frac{\partial E(k)}{\partial t},$$

where the lower integration limit k_{min} corresponds to the wall diameter. The enstrophy transfer rate $\eta(k)$ is evaluated similarly from the enstrophy spectrum $Z(k) = k^2 E(k)$. The time evolution of $\varepsilon(k)$ and $\eta(k)$ during the period when $E(k)$ shows a power-law scaling is shown in Fig. 3 (b). Both in the energy and enstrophy, the transfer rates are maximized at 25 μs when the density configuration changes drastically from separated vortex patches to a single-peak distribution.

These spectra shows the characteristic features of 2D turbulence: The enstrophy is transferred upward in the wave-number space with $k \geq k_{inj}$, while the energy cascades toward lower wave-numbers and its transfer rate is maximized around k_{core} at each time. In particular, over the wide range of $k > 1500$, $\eta(k)$ is almost constant as assumed in the 2D turbulence theory [7]. The rate is estimated as $\eta \approx (0.52 - 2.2) \times 10^{14}$ s^{-3} in Fig. 3 (b). By combining the η and the effective viscosity ν evaluated in the previous section, the dissipative scale l_d is estimated to be 0.57±0.07 mm according to the expression $l_d \approx \eta^{-1/6}\nu^{1/2}$ [7,13]. This length is consistent with the thickness of the filamentary structure at the end of spiral arms shown in Fig. 1, and in the wave-number space, this scale $k = k_d \approx 5500$ corresponds to the upper limit of the power-law scaling in $E(k)$ as shown in Fig. 3 (a).

In contrast to the large wave-number region, in the intermediate scale $k_{inj} \leq k \leq 1500$, $\eta(k)$ decreases to zero around k_{inj} from a constant value at $k > 1500$, which indicates the inhibition of the enstrophy cascade. This observation corresponds to the vortex dynamics observed in Fig. 1, i.e., the filamentation of vortex structures is limited to the outside region of the patches. The constraint of the enstrophy cascade by the coherent vortices has been observed by numerical simulations [15]. This breakdown of the cascade model is considered as a reason why the power index of the energy spectrum $E(k)$ is larger than the theoretical prediction of $\alpha = 3$ [7].

5. Wavelet Analysis of Turbulent Structures

From the preceding analysis based on the Fourier expansion, it has been confirmed that the observed relaxation process proceeds qualitatively according to the enstrophy cascade process proposed by the 2D turbulence theory [7]. However, there remains uncertainty in understanding how the spectral dynamics is connected to the vortex dynamics in the physical space. This uncertainty is attributed to the inherent nature of the Fourier transform that loses the information on the spatial coordinates of the vortex structures. In order to resolve this difficulty, in this section, we

apply the wavelet analysis to the same data set, and investigate the spectral transport in connection with the vortex dynamics in the physical space.

5.1 Multiresolution analysis of density distribution

First, we decompose the density distribution $n(x, y)$ into an orthogonal wavelet series from the smallest scale $2^{-(J-1)}$ to the largest scale 2^0 (where $J = \log_2 \sqrt{N} = 9$ and N is the total pixel number 512×512) using a two-dimensional multiresolution analysis [9, 12] given as

$$n(x,y) = \tilde{n}^0_{0,0}\phi^0_{0,0}(x,y) + \sum_{j=0}^{J-1}\sum_{i_x=0}^{2^j-1}\sum_{i_y=0}^{2^j-1}\sum_{\mu=1}^{3}\tilde{n}^{\mu,j}_{i_x,i_y}\psi^{\mu,j}_{i_x,i_y}(x,y),$$

$$\phi^j_{i_x,i_y}(x,y) = \phi^j_{i_x}(x)\phi^j_{i_y}(y), \psi^{1,j}_{i_x,i_y}(x,y) = \phi^j_{i_x}(x)\psi^j_{i_y}(y),$$

$$\psi^{2,j}_{i_x,i_y}(x,y) = \psi^j_{i_x}(x)\phi^j_{i_y}(y), \psi^{3,j}_{i_x,i_y}(x,y) = \psi^j_{i_x}(x)\psi^j_{i_y}(y),$$

where $\phi^j_{i_x}(x)$ and $\psi^j_{i_x}(x)$ are the scaling function and the corresponding wavelet, respectively. Due to the orthogonality, the wavelet coefficient $\tilde{n}^{\mu,j}_{i_x,i_y}$ at scale 2^{-j} and position (i_x, i_y) is given by $\tilde{n}^{\mu,j}_{i_x,i_y} = \left\langle n, \psi^{\mu,j}_{i_x,i_y}\right\rangle = \int n(\mathbf{r})\psi^{\mu,j}_{i_x,i_y}(\mathbf{r})d\mathbf{r}$, and $\tilde{n}^0_{0,0} = \left\langle n, \phi^0_{0,0}\right\rangle$ corresponds to the mean value of the density.

In this paper, we employ the Coiflet order 12 wavelet in terms of compact-support, symmetry, smoothness, the number of vanishing moments and calculation efficiency [9, 16]. The inner product $\langle\cdot,\cdot\rangle$ is performed with the periodic boundary condition, so that in the low wave-number range the shape of the spectrum is different from that of the spectra shown in Fig. 3 (a) which were calculated with the experimentally imposed boundary condition. Nevertheless, as far as we examine the spectra in the wave-number space above k_{inj}, the spectral structure is confirmed to be consistent with the previous one.

5.2 Spatial dynamics of enstrophy spectrum

From the wavelet coefficients $\tilde{n}^{\mu,j}_{i_x,i_y}$ thus obtained, we evaluate the spatial distribution of the enstrophy spectrum $\tilde{Z}_2(\mathbf{x}, k_j)$ of wave number $k_j = k_0 2^j$ at coordinate $\mathbf{x} = (i_x, i_y)2^{9-j}\Delta x$ as follows [16, 17]:

$$\tilde{Z}_2(\mathbf{x}, k_j) = \frac{1}{2}\left(\frac{e}{\varepsilon_0 B_0}\right)^2 \sum_{\mu=1}^{3}(\tilde{n}^{\mu,j}_{i_x,i_y})^2 \Big/ A_j,$$

where

$$A_j = \Delta k_j \Delta x_j^2,$$

$$\Delta x_j = 2^{9-j}\Delta x, \quad \Delta k_j = \sqrt{k_{j+1}k_j} - \sqrt{k_j k_{j-1}}.$$

$\Delta x = 0.1$ mm is the smallest resolvable scale on the CCD image, and k_0 is determined by the filtering property of the Fourier-transformed wavelet and scaling function. $\tilde{Z}_2(\mathbf{x}, k_j)$ is defined as the density of the enstrophy per unit area Δx_j^2 and per unit wave-number range Δk_j, so that $\sum_\mu (\tilde{n}^{\mu,j}_{i_x,i_y})^2$ is divided by the factor A_j [17].

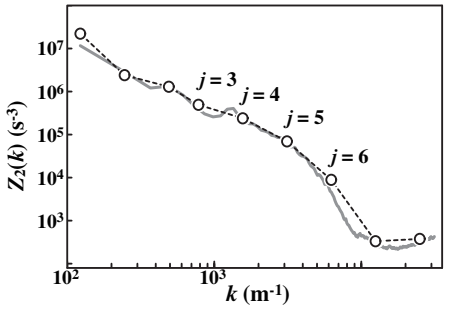

Fig. 4 Enstrophy spectra obtained from the wavelet coefficients (○ + dashed line) and Fourier coefficients (solid grey line) of the density distribution observed at t=31μs.

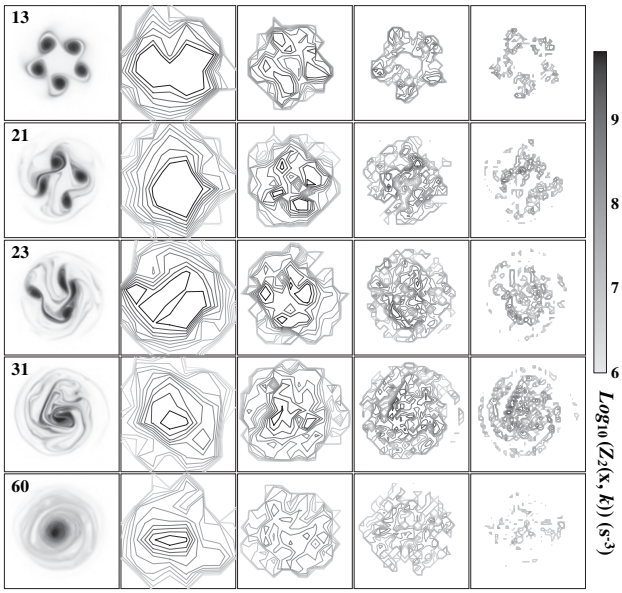

Fig. 5 Contours of the the local enstrophy spectrum $\tilde{Z}_2(\mathbf{x}, k_j)$ for scales j=3-6 corresponding to the density distributions at each time step (left panels). $\tilde{Z}_2(\mathbf{x}, k_j)$ is plotted in a logarithmic scale and the greyscale of contours is proportional to the amplitude.

The spectrum obtained from the wavelet coefficients corresponds to the Fourier-based spectrum $Z_2(k)$, as shown in Fig. 4. Here, the wavelet-based enstrophy spectrum is obtained by summing $\tilde{Z}_2(\mathbf{x}, k_j)$ over all positions, as $\tilde{Z}_2(k_j) = \sum_{i_x,i_y}\tilde{Z}_2(\mathbf{x}, k_j)\Delta x_j^2$. $\tilde{Z}_2(k_j)$ agrees quite well with the $Z_2(k)$, and the scales j=3-6 correspond to the inertial range $k_{inj} \le k \le k_d$.

The contour of the local enstrophy spectrum $\tilde{Z}_2(\mathbf{x}, k_j)$ for scales j=3-6 at each time step is plotted in Fig. 5 together with the corresponding density distribution. The vortex patches are characterized by $\tilde{Z}_2(\mathbf{x}, k_j)$ at j=4, and those coherent properties, spatial locality and high vorticity, are retained throughout the merging process among the patches ($13 \le t \le 31$ μs). At smaller scales of j=5-

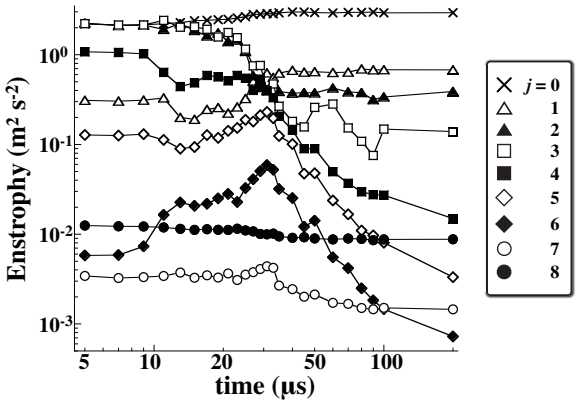

Fig. 6 Time evolution of the enstrophy at each length-scale j=0 (×), 1 (△), 2 (▲), 3 (□), 4 (■), 5 (◊), 6 (⧫), 7 (○), 8 (●).

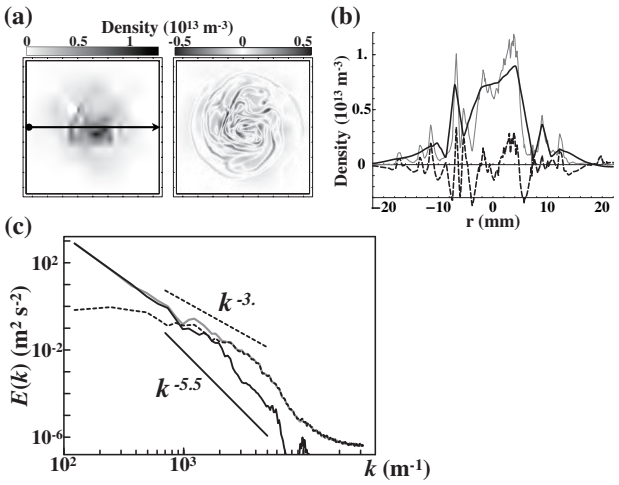

Fig. 7 An example of the extraction result with the threshold of 88.2%. (a) 2D profiles of the coherent component $n_C(x,y)$ (left) and the filamentary component $n_F(x,y)$ (right). (b) 1D profiles of the density distribution $n(x,0)$ (gray line), $n_C(x,0)$ (solid line) and $n_F(x,0)$ (dashed line) along the chord $y = 0$. (c) Energy spectra of n (gray line), n_C (solid line) and n_F (dashed line).

6, $\tilde{Z}_2(\mathbf{x}, k_j)$ is dominant in the interacting region of the patches, and extends spatially along with the filamentation of vortex structures. At the end of the merging process at t =31 μs, while the scales j=5-6 are developed the most extensively, $\tilde{Z}_2(\mathbf{x}, k_j)$ at j=3 is sharpen accompanied by the formation of a single-peaked distribution. In the decaying phase at t >31 μs, the amplitude of $\tilde{Z}_2(\mathbf{x}, k_j)$ at j=3 is concentrated in the central core region, and the enstrophy at scales j=4-6 decrease due to the decay of the fine-scale structures.

The time evolution of the enstrophy $\tilde{Z}_2(k_j)$ at each length-scale is shown in Fig. 6. Throughout the merging process, while $\tilde{Z}_2(k_j)$s at j=2-3 decrease, $\tilde{Z}_2(k_j)$ at j=4 remains almost constant. At smaller scales of j=5-6, $\tilde{Z}_2(k_j)$s show a rapid increase and reach the maximum at 31 μs, like the palinstrophy shown in Fig. 2. This temporal behavior is consistent with the observation of Fig. 5. The successive change of the enstrophy at each length-scale supports the physical interpretation that the enstrophy cascade process proceeds through the filamentation of the vortex structures.

5.3 Effect of coherent vortices on spectrum

As shown in Sec. 4, a long-time persistence of the coherent patches inhibits the cascade of the enstrophy, and, as observed in numerical studies [15], this influence causes the slope of the energy spectrum $E(k)$ to be steeper than the theoretical prediction of k^{-3} [7]. In this section, we examine contributions of the coherent vortices to the energy spectrum by extracting those components from the density distribution [18].

To extract coherent vortices from a turbulent field, various methods have been proposed, a lot of which is performed by clipping the vorticity field using a threshold criterion (see Ref. [13] in Sec. 3). However, the clipping method introduces discontinuities in the vorticity distribution and incorporates spurious components to the Fourier spectrum causing a wrong scaling. For this reason, in this paper, we extract the coherent component in terms of wavelet coefficients based on a threshold criterion [18]. Because wavelet coefficient are localized in both physical and wave-number spaces, the influence of the extraction does not reach the overall spectrum profile.

An example of the extraction result is shown in Fig. 7. Here, the threshold is determined as a rate of the enstrophy accounted by the coherent component. In Fig. 7, we reconstruct the coherent component $n_C(x,y)$ from the largest coefficients containing 88.2% of the total enstrophy (6×10^8 m^2/s^2), and the filamentary component $n_F(x,y)$ are constructed from the remaining coefficients. The reason for this discrimination is discussed later. Due to the orthogonality of the wavelet functions, the density distribution $n(x,y)$ can be decomposed as $n(x,y) = n_C(x,y) + n_F(x,y)$. The 2D and 1D profiles (Fig. 7 (a, b)) demonstrate a clear contrast between the bulk distribution of n_C and the highly structured distribution of n_F. Each energy spectrum (Fig. 7 (c)) shows the power-law scaling $E(k) \propto k^{-\alpha}$ with $\alpha = 5.5$ for n_C, and $\alpha = 3$ for n_F over a wide domain in the wave-number space, which is consistent with the theoretically expected index [7].

In the present study, we cannot determine an appropriate threshold based on a definite criterion [18]. Therefore we carry out the separation with various trial values of threshold ranging from 80 to 100%, and compare the shapes of the spectra for the coherent and filamentary components. Comparison is made in Fig. 8 for each component in terms of the power index α estimated from a linear least-square fit to log-log plot of the energy spectrum $E(k) \propto k^{-\alpha}$ in the wave-number region of $700 \leq k \leq 5000$.

The slope of the spectrum for the filamentary component varies continuously from the power index $\alpha = 3.6$ representing the total spectrum, down to 1 characterizing

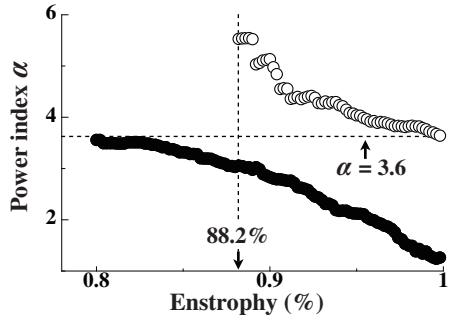

Fig. 8 Power index α of the energy spectrum $E(k) \propto k^{-\alpha}$ in the wave-number region of $700 \leq k \leq 5000$ for coherent ($\circ$) and filamentary ($\bullet$) components at the threshold ranging from 80 to 100%. The vertical dashed line indicates the threshold of 88.2% and the horizontal dashed line indicates the power index of the total spectrum $\alpha = 3.6$.

the white noise (see Eq.(1) for $n(\mathbf{k}) = const.$). In contrast, the spectrum for the coherent component shows the power-law scaling when the threshold is set above 88.2%, and the index decreases continuously from 5.6 down to 3.6 as the threshold increases. For the threshold below 88%, the spectrum becomes oscillatory due to the reduction of the number of wavelet coefficients, and the power-law behavior is lost. The observed transition in the energy spectrum suggests that the appropriate threshold should lie around 88.2%. The distributions plotted in Fig. 7 are based on this discrimination. Although there remain some ambiguities in determining a threshold, this experimental result shows that the steepness of the energy spectrum increases with increasing fraction of the coherent component in the total structure.

6. Conclusion

In this paper, we have examined the relaxation process of 2D turbulence in a magnetized pure electron plasma over a wide range of length scales extending from the injection scale down to the dissipative scale. In the stage characterized by the successive mergers among vortex patches starting from the unstable initial density profile, the Fourier-based analyses have revealed that the spectral dynamics of the energy and enstrophy in the wave-number space exhibits the characteristic features of the 2D turbulence: While the energy is transfered downward, the enstrophy undergoes an upward transport starting from the injection wave-number k_{inj}. In smaller length scales with $k > 3k_{inj}$, the transfer rate of the enstrophy is observed to be constant, and the energy spectrum shows a power-law scaling $E(k) \propto k^{-\alpha}$ in the broad inertial range $k_{inj} \leq k \leq k_d$ with α larger than the theoretical prediction of 3.

This spectral dynamics have been connected directly to the vortex dynamics in the physical space by applying the wavelet analysis to the observed density distribution. Taking advantage of the simultaneous resolution in the physical and wave-number spaces, we have confirmed that the observed enstrophy cascade proceeds through the filamentation process of the vortex structures. Moreover, by extracting the coherent structures from the turbulent field in terms of the wavelet coefficients, we have shown that the coherent vortices make a significant contribution to the steepening of the energy spectrum, and the extracted field has the spectrum following the power-law scaling $E(k) \propto k^{-\alpha}$ with $\alpha \approx 3$ as expected in the 2D turbulence theory.

This research was supported by the Grant-in-Aid for Scientific Research (B) 17340173 of JSPS, by Grant-in-Aid for JSPS Fellows (20-3246) and partly by the collaborative program of NIFS.

[1] C. F. Driscoll, D. Z. Jin, D. A. Schecter and D. H. E. Dubin, Physica C **369**, 21 (2002).
[2] Y. Kiwamoto, K. Ito, A. Sanpei and A. Mohri, Phys. Rev. Lett. **85**, 3173 (2000).
[3] K. S. Fine, A. C. Cass, W. G. Flynn and C. F. Driscoll, Phys. Rev. Lett. **75**, 3277 (1995).
[4] Y. Kiwamoto, N. Hashizume, Y. Soga, J. Aoki and Y. Kawai, Phys. Rev. Lett. **99**, 115002 (2007).
[5] Y. Kawai, Y. Kiwamoto, K. Ito, A. Sanpei, Y. Soga, J. Aoki and K. Itoh, J. Phys. Soc. Jpn. **75**, 104502 (2006).
[6] Y. Kawai, Y. Kiwamoto, Y. Soga and J. Aoki, Phys. Rev. E **75**, 066404 (2007).
[7] R. H. Kraichnan, Phys. Fluids **10**, 1417 (1967). G. K. Batchelor, Phys. Fluids **12** (Suppl.II), 233 (1969).
[8] Y. Kawai and Y. Kiwamoto, Phys. Rev. E **78**, 036401 (2008).
[9] M. Farge, Annu. Rev. Fluid Mech. **24**, 395 (1992). I. Daubechies, *Ten Lectures on Wavelets* (SIAM, Philadelphia, 1992).
[10] A. J. Peurrung and J. Fajans, Phys. Fluids A **5**, 493 (1993).
[11] K. Ito, Y. Kiwamoto and A. Sanpei, Jpn. J. Appl. Phys. **40**, 2558 (2001).
[12] M. Farge, K. Schneider and N. Kevlahan, Phys. Fluids **11**, 2187 (1999).
[13] P. Tabeling, Phys. Rep. **362**, 1 (2002).
[14] D. H. E. Dubin and T. M. O'Neil, Phys. Plasmas. **5**, 1305 (1998).
[15] R. Benzi, G. Paladin, S. Patarnello, P. Santangelo and A. Vulpiani, J. Phys. A **19**, 3771 (1986).
[16] V. Perrier, T. Philipovitch and C. Basdevant, J. Math. Phys. **36**, 1506 (1995).
[17] M. Do-Khac, C. Basdevant, V. Perrier and K. Dang-Tran, Physica D **76**, 252 (1994).
[18] N. K.-R. Kevlahan and M. Farge, J. Fluid Mech. **346**, 49 (1997).